Monthly Notices
of the
ROYAL ASTRONOMICAL SOCIETY

MNRAS **510,** 4166–4179 (2022) https://doi.org/10.1093/mnras/stab3634
Advance Access publication 2021 December 13

Thermal conductivity measurements of macroscopic frozen salt ice analogues of Jovian icy moons in support of the planned JUICE mission

C. González Díaz ,[1]⋆ S. Aparicio Secanellas,[2] G. M. Muñoz Caro,[1]⋆ J. J. Anaya Velayos,[2] H. Carrascosa,[1] M. G. Hernández,[2] V. Muñoz-Iglesias,[1] Á. Marcos-Fernández,[3] O. Prieto-Ballesteros,[1] R. Lorente,[4] O. Witasse[5] and N. Altobelli[4]

[1]*Centro de Astrobiología (CSIC-INTA), Ctra. de Ajalvir, km 4, Torrejón de Ardoz, E-28850 Madrid, Spain*
[2]*Instituto de Tecnologías Físicas y de la Información, Leonardo Torres Quevedo, (ITEFI-CSIC), c/ Serrano 144, E-28006 Madrid, Spain*
[3]*Instituto de Ciencia y Tecnologías de Polímeros (ICTP-CSIC), Juan de la Cierva, 3, E-28006 Madrid, Spain*
[4]*European Space Agency (ESA) - European Space Astronomy Centre (ESAC), Camino Bajo del Castillo, s/n Villafranca del Castillo, E-28692 Villanueva de la Cañada (Madrid), Spain*
[5]*European Space Agency (ESA), European Space Research and Technology Centre (ESTEC), Keplerlaan 1, 2201 AZ, Noordwijk, the Netherlands*

Accepted 2021 December 3. Received 2021 November 8; in original form 2021 September 7

ABSTRACT

The study of thermal properties of frozen salt solutions representative of ice layers in Jovian moons is crucial to support the JUpiter ICy moons Explorer (JUICE) (ESA) and Europa Clipper (NASA) missions, which will be launched in the upcoming years to make detailed observations of the giant gaseous planet Jupiter and three of its largest moons (Ganymede, Europa, and Callisto), due to the scarcity of experimental measurements. Therefore, we have conducted a set of experiments to measure and study the thermal conductivity of macroscopic frozen salt solutions of particular interest in these regions, including sodium chloride (NaCl), magnesium sulphate ($MgSO_4$), sodium sulphate (Na_2SO_4), and magnesium chloride ($MgCl_2$). Measurements were performed at atmospheric pressure and temperatures from 0 to −70 °C in a climatic chamber. Temperature and calorimetry were measured during the course of the experiments. An interesting side effect of these measurements is that they served to spot phase changes in the frozen salt solutions, even for very low salt concentrations. A small sample of the liquid salt-water solution was set aside for the calorimetry measurements. These experiments and the measurements of thermal conductivity and calorimetry will be valuable to constrain the chemical composition, physical state, and temperature of the icy crusts of Ganymede, Europa, and Callisto.

Key words: conduction – methods: laboratory – planets and satellites: fundamental parameters.

1 INTRODUCTION

Measurements of thermal conductivity in frozen salt solutions as analogues of Jovian icy moons are very scarce in the literature. These moons will be visited in the coming years by the JUpiter ICy moons Explorer (JUICE) (ESA) and Europa Clipper (NASA) missions. JUICE is the first large-class mission in ESA's Cosmic Vision 2015–2025 programme. Planned for launch in 2022 and arrival at Jupiter in 2029, it will spend at least 3 yr making detailed observations of Jupiter and its environment.

In this work, we propose to study the thermal conductivity and calorimetry of frozen solutions containing one of these salts: sodium chloride (NaCl), magnesium sulphate ($MgSO_4$), sodium sulphate (Na_2SO_4), and magnesium chloride ($MgCl_2$). These samples were selected as ice analogues in Jovian moons.

The focus of JUICE is to characterize the conditions that may have led to the emergence of habitable environments among the Jovian icy satellites, with special emphasis on the three ocean-bearing worlds: Ganymede, Europa, and Callisto (Kivelson, Khurana & Volwerk 2002).

Ganymede is the primary scientific target of the mission. With a diameter of about 5260 km, it orbits Jupiter at an average distance of 1.070.400 km. Researchers believe that tidal heating likely occurred on Ganymede and drove tectonic activity (Cameron et al. 2018). There is evidence for a subsurface layer of salt water under its icy surface (Clark 1980; Golombek & Allison 1981; Parmentier et al. 1982; Noll et al. 1996; McCord et al. 1997, 1998a, 2001; Collins, Head & Pappalardo 1998; Pappalardo et al. 1998; Hendrix, Barth & Hord 1999; Prockter, Pappalardo & Head III 2000; McCord, Hansen & Hibbitts 2001; Kivelson et al. 2002; Showman, Mosqueira & Head 2004; Patterson et al. 2010; Sohl et al. 2010; Pettinelli et al. 2015; Heggy et al. 2017). The depth limits of these oceans are unknown and how it interacts with both the deep interior of Ganymede and the icy crust above it. Finding out more about Ganymede's ice and liquid layers, including its composition and conductivity, is a main objective of JUICE since the ocean might be habitable. The mission will use an ice-penetrating radar to probe the moon's subsurface structure down to a depth of about 9 km. Europa is the second target of JUICE. With a diameter of 3121.6 km and average distance from Jupiter of 670.900 km, tidal heating is important in this moon. It hosts an ocean beneath its frozen outer shell and offers the best habitability conditions within the Jovian satellites (Fink, Dekkers & Larson 1973; Fink et al. 1973; Kargel 1991; Carlson et al. 1996, 1999a; McCord

---

⋆ E-mail: cristobal.g.diaz@csic.es (CGD); munozcg@cab.inta-csic.es (GMMC)

Published by Oxford University Press on behalf of Royal Astronomical Society

Table 1. Salt systems and concentrations selected for this study based on phase diagrams reported in the literature (Li et al. 2016; Chou, Seal & Wang 2013; Brand et al. 2009), and references therein.

Salt system	Eutectic temperature (°C)	Initial concentration (wt. per cent)
NaCl	−21.1	1.2, 23.16 (eutectic) in Fig. 4
$MgSO_4$	−3.7	17 (eutectic) in Fig. 7
Na_2SO_4	−1.3 and −3.5	4.15 (eutectic 1), 12.8 (eutectic 2), 17 in Fig. 10
$MgCl_2$	−33.2	21 (eutectic) in Fig. 13

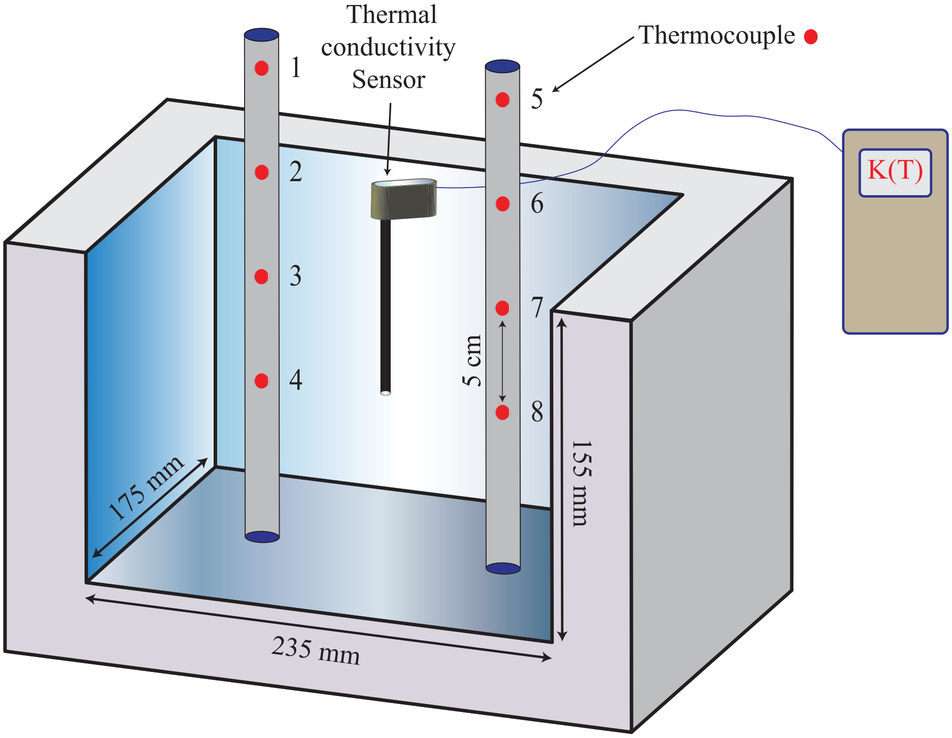

Figure 1. Dimensions of the interior of the EPS box and schematic view showing the positioning of the thermocouples and thermal conductivity sensor.

et al. 1998b; Carlson, Johnson & Anderson 1999b; Kargel et al. 2000; Dalton et al. 2005, 2013; Marion et al. 2005; Orlando, McCord & Grieves 2005; Prieto-Ballesteros et al. 2005; Hansen & McCord 2008). JUICE will explore the chemistry of Europa's water-vapour potential plumes emerging from its young ice crust (Sparks et al. 2016; Roth et al. 2014). Active zones in Ganymede and Europa could provide a way to exchange material and heat between the moon's surface and the ocean beneath (Grasset et al. 2013). JUICE will also study Callisto. This moon has a diameter of 4821 km and average orbital radius of 1.883.000 km. Callisto experienced lower tidal heating than Ganymede and is exposed to lower radiation field than the other Galilean moons. The presence of an ocean beneath its rocky and ice surface is not as clear (Clark 1980; Schenk 1993, 1995, 2002; Showman & Malhotra 1999; McCord et al. 1997, 1998a; Greeley et al. 2000; Zimmer, Khurana & Kivelson 2000; Sohl et al. 2010; Pettinelli et al. 2015; Heggy et al. 2017). Callisto has an old cratered surface and is geologically stable compared to the other Galilean moons (Anderson et al. 2001; Kuskov & Kronrod 2005). For more details on JUICE mission, see https://sci.esa.int/web/juice. The JUICE and Europa Clipper missions incorporate a radar to explore the surface and subsurface of the moons. Clipper will also measure temperature changes on Europa's surface and a mass spectrometer to determine the surface composition. Further information can be found in https://www.jpl.nasa.gov/missions/europa-Clipper. In this paper, the measurements of temperature and thermal conductivity of ice analogues containing salts with the different concentrations will serve as input for thermodynamical models of Jovian icy moons. These models will be developed to interpret the volume of data from these missions. The applicability of the data reported in this paper to Jovian icy moons requires an extrapolation of the curves to lower temperatures. Unfortunately, there is no literature reporting similar measurements at lower temperatures that we could use as a reference. However, for the pure water case there are some works that measure the thermal conductivity at temperatures below −50 °C (Klinger 1980; Slack 1980; Andersson & Inaba 2005). These authors report an exponential increase of thermal conductivity as the temperature decreases. In addition to the temperature thickness of the different liquid/ice layers of the moon, the thermal conductivity is required as input for estimation of heat transfer as a function of depth. The thermal conductivity value depends on the composition and physical properties of the salt ice and changes as a function of the temperature.

2 EXPERIMENTAL PROTOCOL

In this section, the sample production is described and the characterization of the macroscopic ice samples containing salts. The

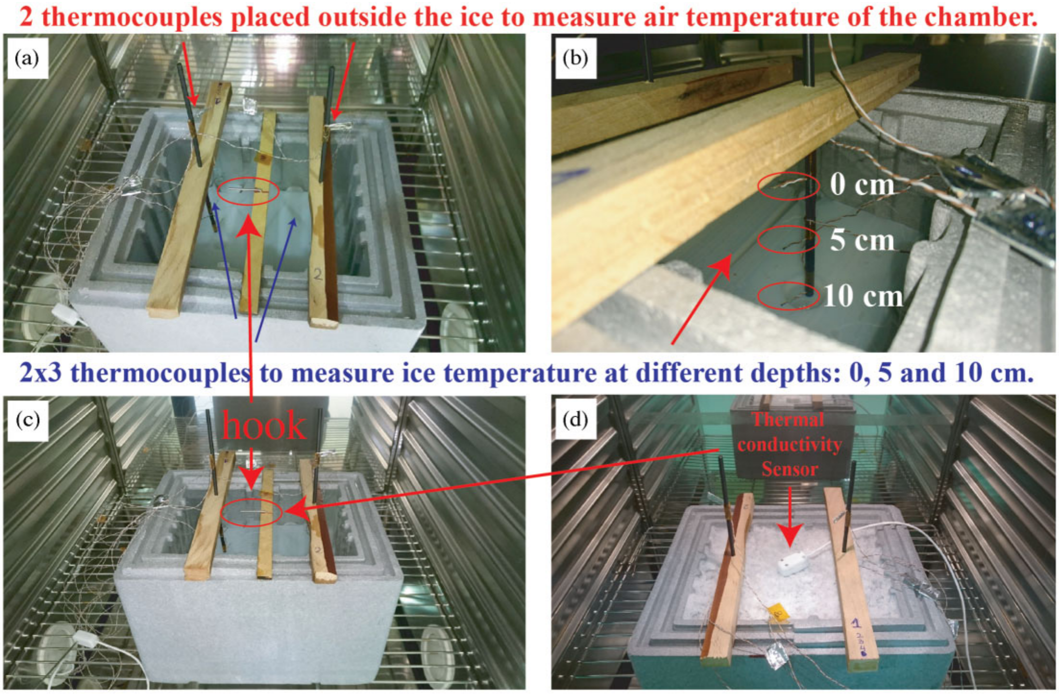

Figure 2. Schematic view of the ice sample formation using the climatic chamber and the EPS box. (a) Salt solution in the EPS box placed inside the climatic chamber showing the thermocouple arrays, (b) thermocouples positioned at different depths in the salt solution, (c) the hook used as guide, to be replaced by the thermal conductivity sensor, and (d) thermal conductivity sensor in the salt solution.

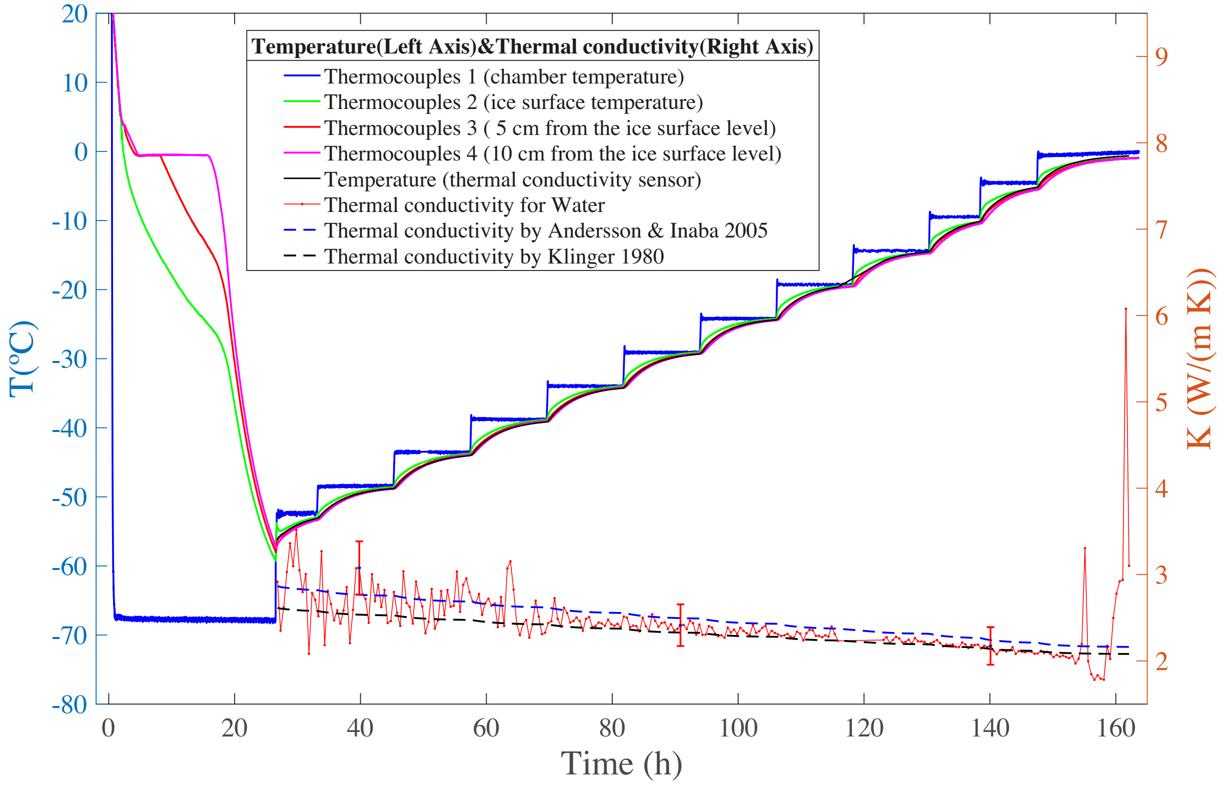

Figure 3. Thermal conductivity and temperature values measured by thermocouples and thermal conductivity meter for pure H_2O ice as a function of time. Previously published thermal conductivity values by Andersson & Inaba (2005) (dashed blue trace) and by Klinger (1980) (dashed black trace). To link the temperature values to their corresponding thermal conductivity values, for instance at 100 h, an imaginary vertical line should be projected from the thermal conductivity value to the temperature values on top.

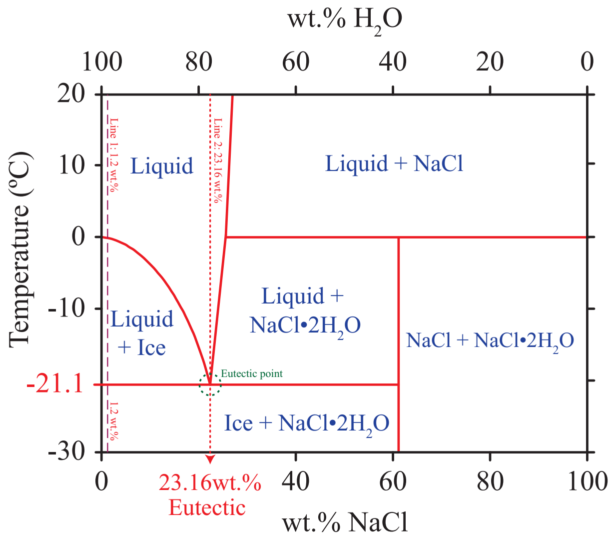

Figure 4. Phase diagram for the NaCl + H_2O solution. Redrawn after Li et al. (2016), and references therein.

protocols for temperature, thermal conductivity, and calorimetry measurements are presented. Macroscopic frozen salt solutions are of special concern in three of the largest Jovian Moons with an ice crust: Ganymede, Europa, and Callisto. Analogue solutions were made according to the literature input requirements. The chemical components of the samples are: sodium-chloride (NaCl), magnesium-sulphate ($MgSO_4$), sodium sulphate (Na_2SO_4), and magnesium chloride ($MgCl_2$) with different concentrations, see Table 1. The water used to fabricate the ice samples is 'ultrapure' water of 'Type 1' (Milli-Q). The chemicals Sodium chloride 99.5–100.5 per cent, AnalaR NORMAPUR® ACS, Reag. Ph. Eur. analytical reagent, Magnesium chloride, anhydrous ≥ 98 per cent, high purity, Sodium sulphate, anhydrous 98.5–101.0 per cent, AnalaR NORMAPUR® Reag. Ph. Eur. analytical reagent, and Magnesium sulphate, anhydrous 99–100.5 per cent USP salts were purchased from AVANTOR. For each ice sample, temperature and thermal conductivity were measured. For the temperature measurement, eight thermocouples of 'type T', 'class 1' were placed in two rods, see Figs 1 and 2. The temperature was recorded every 30 s. For each rod, one was kept outside the sample to measure the temperature in the interior of the chamber and the other three were embedded in the sample at different depths (at 0, 5, and 10 cm from the ice surface level). The thermal conductivity was measured with a commercial device TEMPOS–thermal properties analyser from 'METER Group'. The TR-3 sensor of TEMPOS was used to measure the thermal conductivity K of the frozen salt solutions. This single-needle TR-3 sensor measures thermal conductivity and thermal resistivity. The TR-3 is primarily designed for soil and other granular or porous materials. This single-needle sensor is based on the hot-wire probe method, consisting of a needle with a heater and temperature sensor inside. The sensor can measure temperatures in the range of $-50\,^{\circ}$C to $+150\,^{\circ}$C with a precision of $0.001\,^{\circ}$C. The sensor dimensions are 100 mm long and 2,4 mm diameter. The thermal conductivity measurement range of this device is 0.1–4.0 ± 10 per cent W/(m·K). The peaks in the thermal conductivity measured during phase changes correspond to

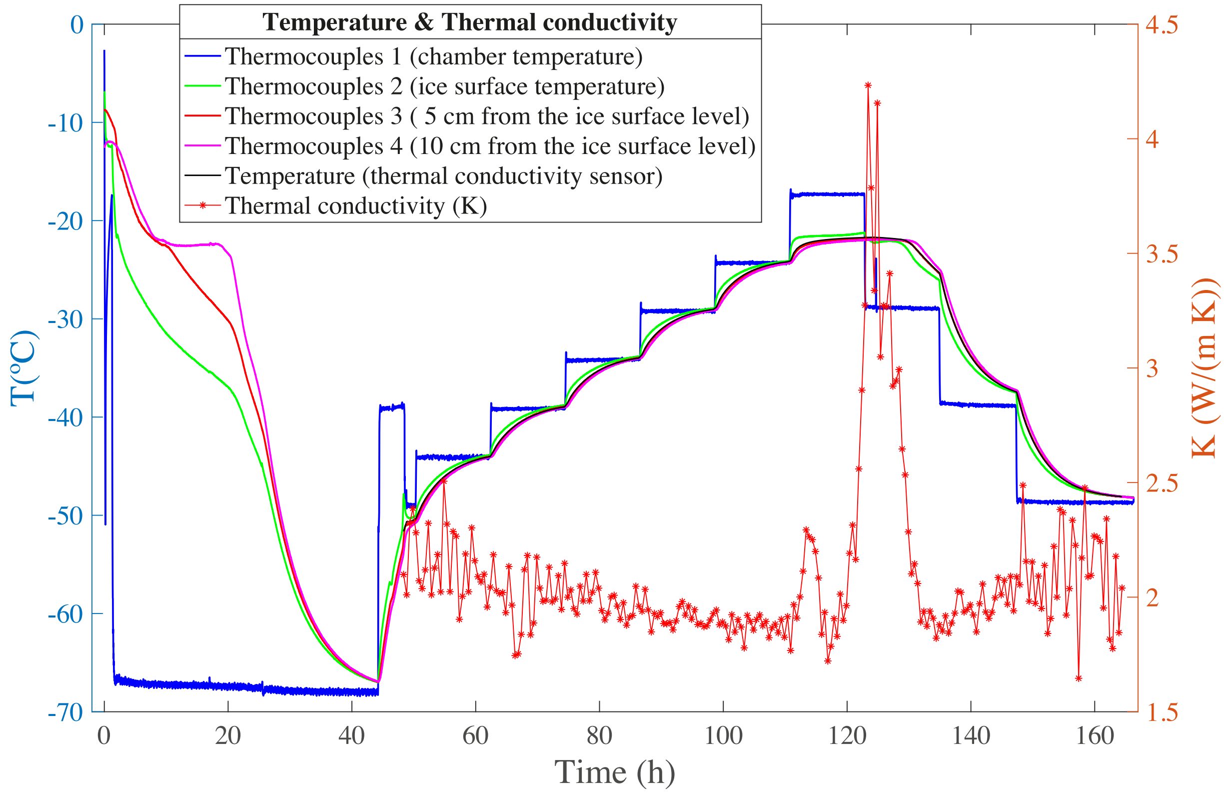

Figure 5. Thermal conductivity (right axis) and temperature (left axis) values measured by thermocouples and thermal conductivity meter for eutectic (23.16 wt. per cent) NaCl + H_2O ice as a function of time. To link the temperature values to their corresponding thermal conductivity values, for instance at 100 h, an imaginary vertical line should be projected from the thermal conductivity value to the temperature values on top.

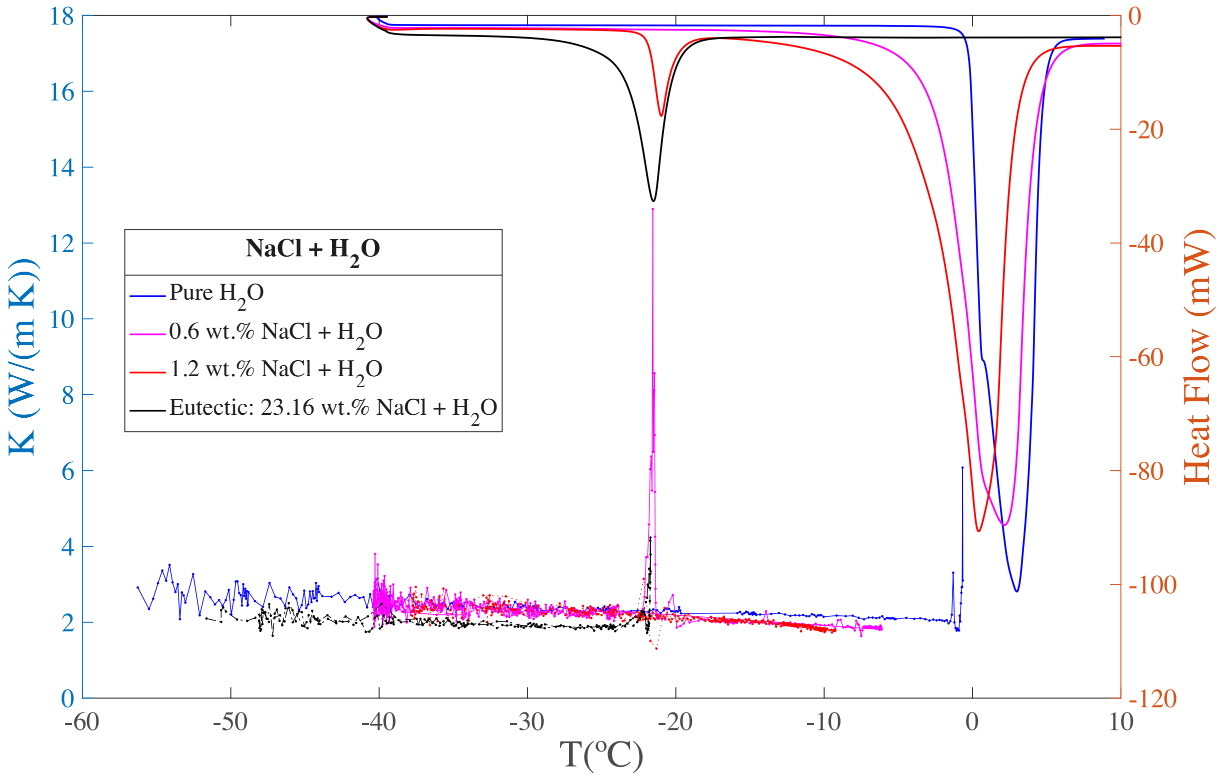

Figure 6. Thermal conductivity (left axis) and calorimetry (right axis) measurements for NaCl + H_2O with different NaCl concentration. Blue trace is pure H_2O. Red trace is 1.2 wt. per cent NaCl + H_2O. Black trace is (Eutectic): 23.16 wt. per cent NaCl + H_2O.

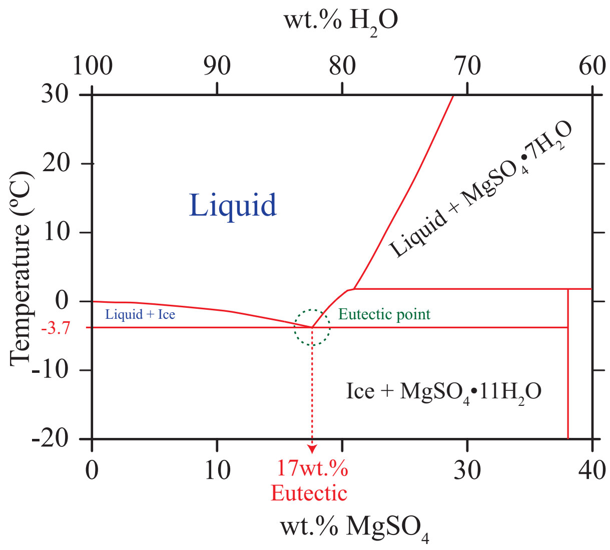

Figure 7. Phase diagram for the eutectic 17 wt. per cent $MgSO_4$ + H_2O solution. Redrawn after Chou et al. (2013), and references therein.

unrealistically high values of the thermal conductivity, for instance see Fig. 3 between 153 and 162 h, at 0 °C. These peaks served to spot phase changes as they are caused by a change in the temperature during the phase change that the sensor interprets as a large variation of the thermal conductivity. In addition, for solutions at the phase change temperature, convection induces temperature variations and the thermal conductivity measurements may have large uncertainties. In Fig. 3 to clarify the precision of the thermal conductivity sensor [± 10 per cent W/(m·K)] relative to the overall measurements, three error bars were placed at the beginning, middle, and near the end of the experiment. Since the error is always 10 per cent of the thermal conductivity measurement, the error bars for all the points have not been plotted to avoid data overload in the figure. The error bars for the thermal conductivity temperature sensor have not been added since the error is only ±0.001 °C. Moreover, the temperature is also doubly measured with two arrays of four thermocouples each (two thermocouples per position) to further reduce the temperature error. The impurities in the samples that could introduce any error in the thermal conductivity measurements are insignificant since they are negligible compared to the amount of water or salt used to manufacture them. For instance, for the eutectic sample of NaCl (23.16 wt. per cent NaCl + H_2O) 5 litres of 'ultrapure' water (Milli-Q) and 1510.7 g of NaCl were used. The error of the balance used is 0.01 g, a clearly negligible value for the sample amounts used in our experiments that corresponds to 0.0006 per cent of the salt weight, errors of this order are estimated for the other experiments.

A solution containing a given salt concentration was prepared after stirring and placed in the interior of an expanded polystyrene (EPS) dry box, see Figs 1 and 2. Fig. 1 shows the dimensions of the interior of the EPS dry box and schematic view showing the two rods with positioning of the eight thermocouples and the thermal conductivity sensor used to measure the temperature and the thermal conductivity of the ice samples. Besides, the thermal conductivity and the temperature, a small sample of the liquid salt-water solution was set aside for the calorimetry measurements to determine the changes in energy of the samples by measuring the heat exchanged with the surroundings when the temperature is increasing/decreasing. Heat flow variations with the temperature were measured with the µDSC7 evo calorimeter (SETARAM Instrumentation), with a

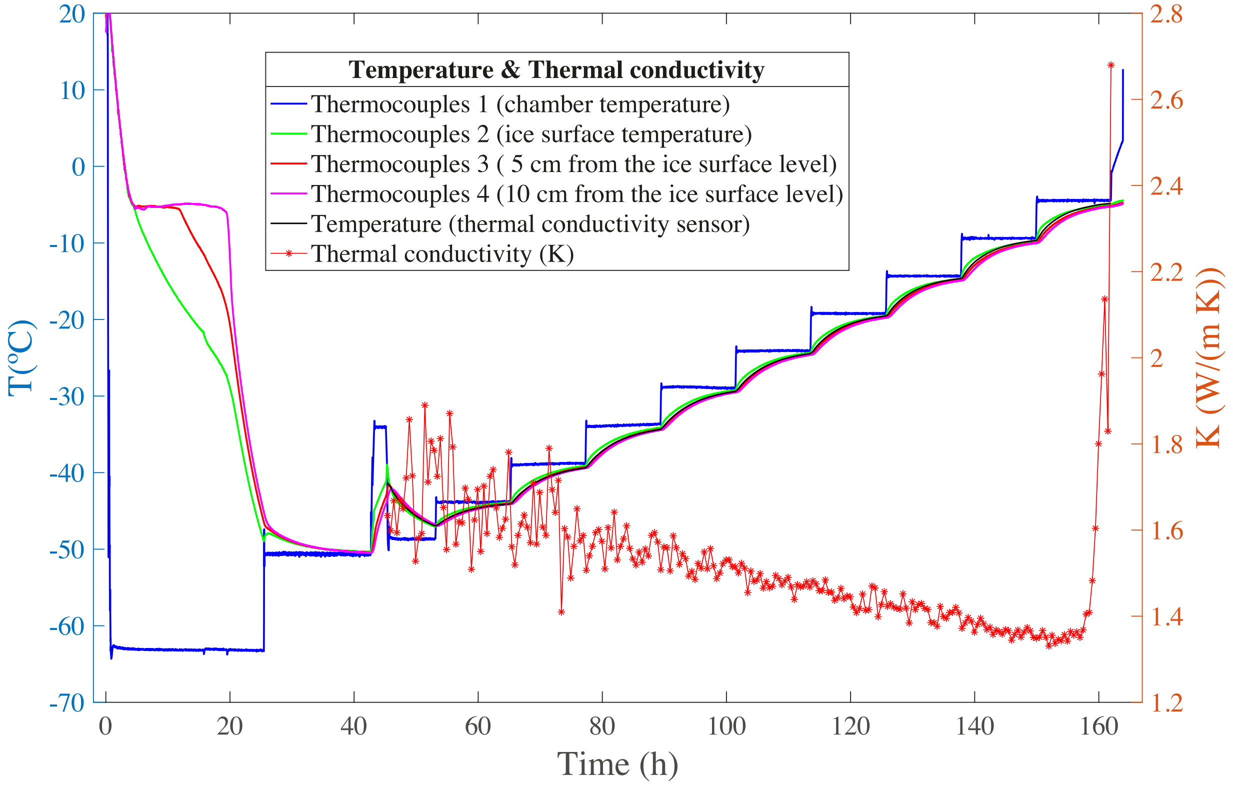

Figure 8. Thermal conductivity (right axis) and temperature (left axis) values measured by thermocouples and thermal conductivity meter for eutectic (17 wt. per cent) $MgSO_4 + H_2O$ ice as a function of time. To link the temperature values to their corresponding thermal conductivity values, for instance at 100 h, an imaginary vertical line should be projected from the thermal conductivity value to the temperature values on top.

signal-to-noise ratio of 0.4 µW and a resolution of 0.02 µW. The reference cell was left empty in all the runs. The protocol for the calorimetry test is the following: (1) the sample solution is cooled down from 25 °C to −40 °C at the speed of −5 °C/min, then it is kept at −40 °C during 20 min and finally, the sample solution is heated up from −40 °C to 20 °C at 1 °C/min. For the $MgCl_2$, since the eutectic point at −33.2 °C, is closer to the limits of our previous calorimeter device, −40 °C, the thermal transitions were analysed by differential scanning calorimetry (DSC) on a Mettler Toledo DSC 822e calorimeter (Schwerzenbach) equipped with a liquid nitrogen accessory. A sample weighing approximately 20 mg in an aluminium pan was cooled from 25 °C to −90 °C at a rate of 10 °C/min, maintained for 7 min at this temperature and reheated from −90 °C to 25 °C at a rate of 10 °C/min. All scans were carried out under a constant nitrogen purge of 30 mL/min. Phase changes were taken as the onset of the transition for sharp peaks, and as the extremum peak temperature for broad-bands, respectively (Lin et al. 2013).

To perform the experiments a climatic chamber was used, manufactured by Votsch (model: VTR 7033/S). The chamber temperature can operate in the temperature range from −70 °C to 120 °C and temperature ramps of 7.5 K/min (heating) and 6.5 K/min (cooling) can be conducted. The humidity ranged between 10 per cent and 98 per cent and the refrigerant R404A was used. The expected ice temperatures in Jovian moons are well below −100 °C. Due to experimental limitations, measurements were performed at atmospheric pressure and temperatures from 0 to −70 °C, and the thermal conductivity could only be measured from 0 °C to −50 °C. The climatic chamber does not allow inclusion of volatile species in the ice. Large blocks of salt ice can be grown inside the climatic chamber and the scientific equipment (thermocouples and the thermal conductivity sensor) is connected to the chamber via a port, see Fig. 2. It allows introducing samples and sensors inside the chamber while the electronics remain out of the climatic chamber. Fig. 2 shows photographs of the ice sample formation using the climatic chamber and the EPS box. A hook with similar dimension as the thermal conductivity sensor was inserted in the solution as guide to the thermal conductivity sensor. Once the salt solution is frozen, this hook is replaced by the thermal conductivity sensor.

As soon as the EPS box containing the salt solution is placed in the interior of a climatic chamber, the temperature of the climatic chamber is set to the minimum temperature range, around −70 °C during 1–2 d, depending of the salt solution, to permit freezing of the complete sample volume. This can be seen for instance in Fig. 3, where the thermocouple sensors 1 (blue line) and 5 (magenta line) are shown. These sensors are located outside the EPS box and were used to record the ambient temperature of the climatic chamber, displaying a plateau at around −70 °C during the first 24 h of the experiment. When the whole salt solution was frozen, a heating ramp was programmed until the salt solution reached the eutectic temperature. To allow potential structural changes in the ice that may require more time, we introduced ‘steps’ in temperature, where the temperature was kept intentionally constant at a given temperature value, for instance see Fig. 3. The duration in time of the ‘steps’ was not the same for all the experiments or salt solutions studied. Not all the salt solutions took the same amount of time to reach the temperature due to their lower or higher thermal conductivity and specific heat.

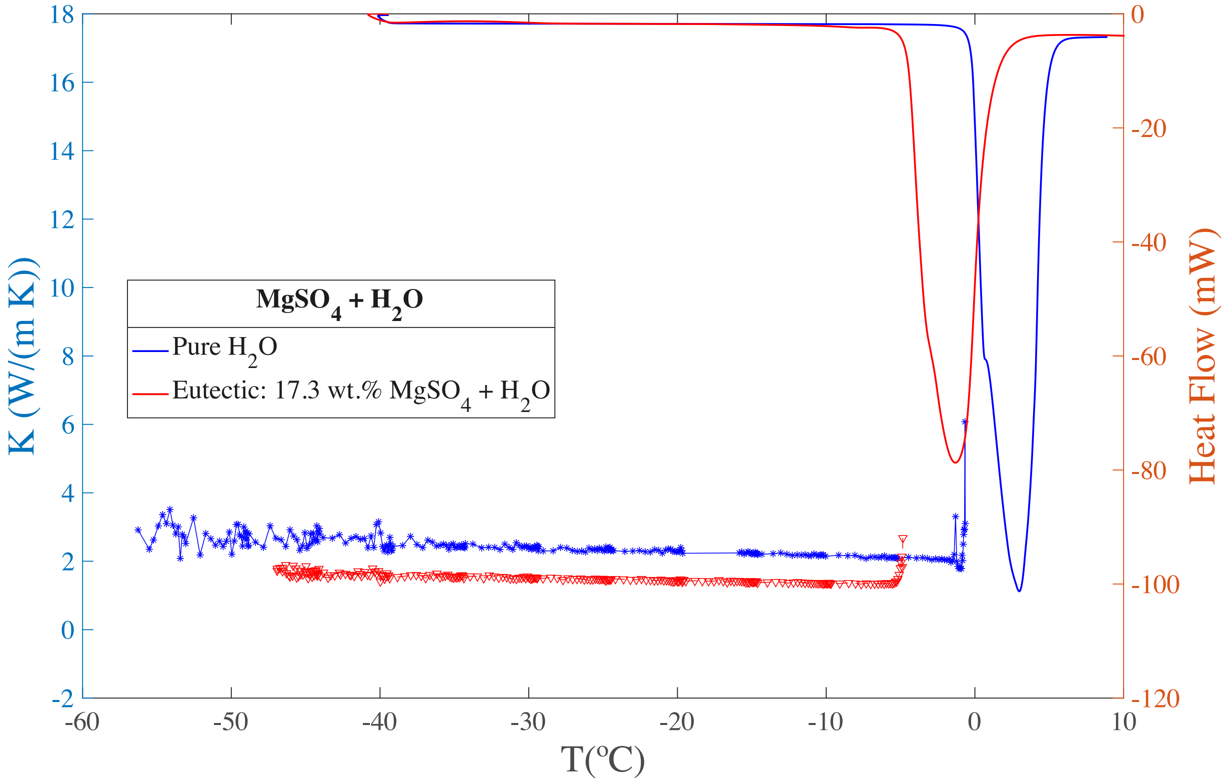

Figure 9. Thermal conductivity (left axis) and calorimetry (right axis) measurements for $MgSO_4$ + H_2O with eutectic $MgSO_4$ concentration. Blue trace is pure H_2O. Red trace is eutectic 17.3 wt. per cent $MgSO_4$ + H_2O.

3 EXPERIMENTAL RESULTS

3.1 Pure H_2O ice

This experiment served to test the performance of the set-up as the results can be compared with the literature values. The phase change of water from liquid to solid can be seen in Fig. 3, where the thermocouple sensors show a plateau at 0 °C during the first hours of the experiment. The duration of the plateau increases as the thermocouples are placed deeper in the interior of the EPS box. This is the case of thermocouples 4 and 8 placed at a depth of 10 cm from the ice surface level. At these positions, the water solution remains in the liquid state for about 16 h. These plateaus or lower rate of cooling illustrate that the heat is being released as water ice continuously freezes, which is the result of slowing down the cooling rate of water.

Once the water solution has fully solidified, heat is no longer released by solidification and the water ice cools down rapidly. Temperature drops from 0 °C to −60 °C in 10 h. Upon warming, the water ice melts. This is shown by a long period of constant temperature due to the endothermic melting. The temperature of this plateau is at 0 °C in the last step of the experiment between 156 and 165 h.

Fig. 3 also shows the measurements of the thermal conductivity of a pure water ice sample down to −50 °C to verify the correct functioning of the experimental set-up. The temperature measured with the conductivity meter was quantified as 'very similar' to the temperature measured with the deepest thermocouples. The thermal conductivity values are in good agreement with the literature values in this temperature range (Slack 1980; Klinger 1980; Andersson & Inaba 2005; Carey et al. 2018; Bonales, Rodriguez & Sanz 2017) as could be stated by the blue (thermal conductivity by Andersson & Inaba 2005) and black (thermal conductivity by Klinger 1980) dashed line in Fig. 3.

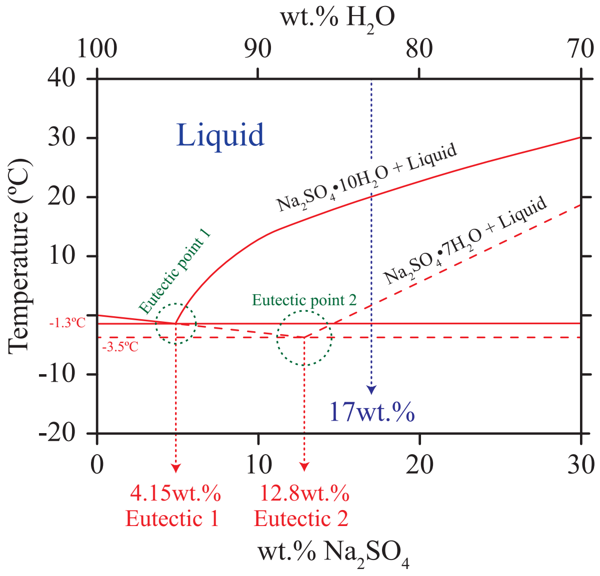

Figure 10. Phase diagram for the Na_2SO_4 + H_2O solution showing stable phase boundaries (solid) and metastable phase boundaries (dashed). E_1 and E_2 are the mirabilite-ice and the $Na_2SO_4 \cdot 7\,H_2O$-ice eutectics, respectively. Redrawn after Brand et al. (2009), and references therein.

Fig. 3 shows few peaks occurring around 0 °C in the thermal conductivity measurement (red traces). These peaks coincide with the phase change from solid to liquid in the H_2O ice. The

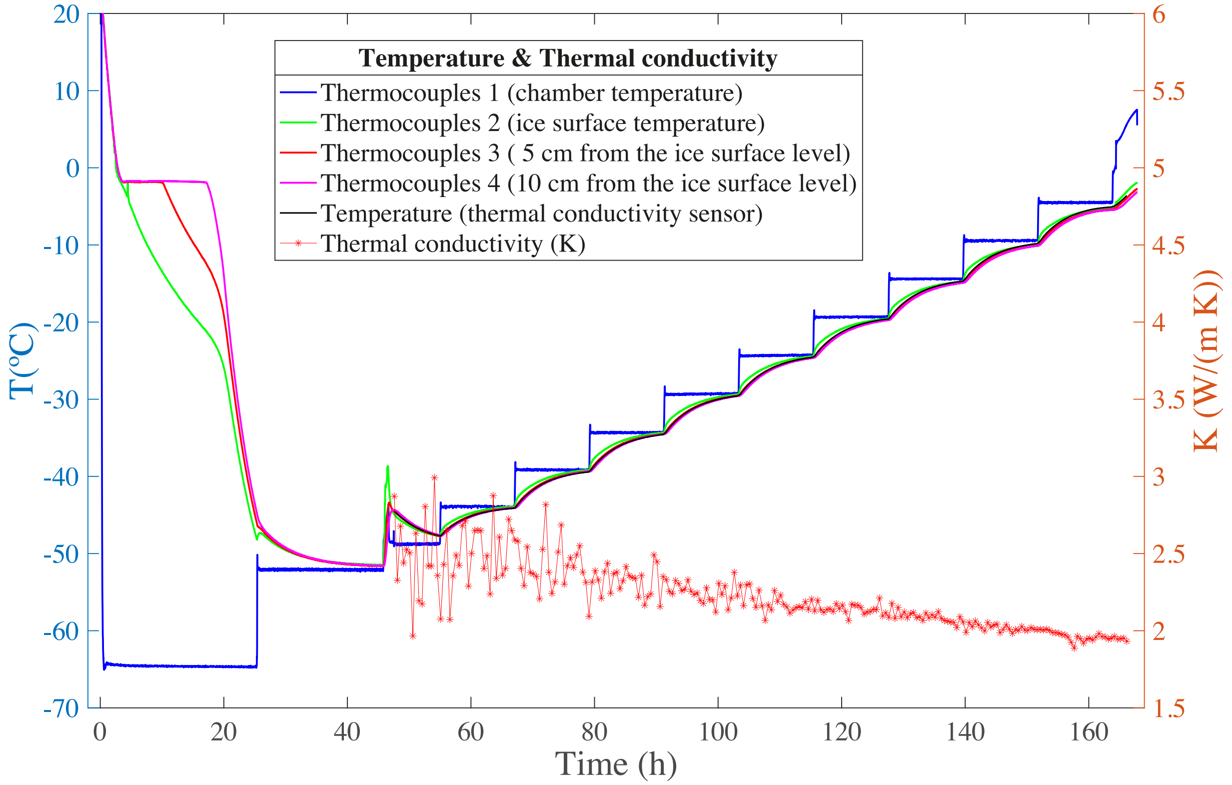

Figure 11. Thermal conductivity (right axis) and temperature (left axis) values measured by thermocouples and thermal conductivity meter for eutectic$_1$ (4.15 wt. per cent) $Na_2SO_4 + H_2O$ ice as a function of time. To link the temperature values to their corresponding thermal conductivity values, for instance at 100 h, an imaginary vertical line should be projected from the thermal conductivity value to the temperature values on top.

temperature ramp displays ‘steps’ in Fig. 3 because the temperature was kept intentionally constant at a given temperature value to allow potential structural changes in the ice that may require more time, see Section 2.

3.2 Sodium chloride (NaCl) solution

From the phase diagram provided in Fig. 4, which is a conventional phase diagram of a NaCl solution, it is found which concentration of the solution will determine which solids will precipitate and the temperature at which equilibrium precipitation first occurs. A phase diagram displays the phases in a multicomponent system as a function of the concentration (wt. per cent) of the components and temperature. The selection of solution concentrations for the freezing/warming experiments was made based on the concentrations at which major phase changes occur in the phase diagram, such as the eutectic temperature and transitions between salt hydrates. The phase diagram can be examined following different vertical lines (dashed red) to illustrate the responses expected with different concentration in our experiments.

From Fig. 4, Line 1: 1.2 wt. per cent describes a temperature change from 20 °C to −30 °C for dilute 1.2 wt. per cent $NaCl + H_2O$ solution; decreasing the temperature starting from 20 °C causes no change in the solution until the temperature goes below the red solid line at slightly below 0 °C, at this point pure H_2O ice starts to develop in the solution and the concentration of the liquid (unfrozen solution) increases until the temperature reaches the eutectic temperature of −21.1 °C for $NaCl + H_2O$. Further down this temperature, no more liquid will be found as it will be pure water ice and the eutectic solid mixture containing pure water ice (77 wt. per cent) and $NaCl{\cdot}2H_2O$ crystals known as hydrohalite (23 wt. per cent). Another solution with an eutectic concentration of 23.16 wt. per cent of NaCl salt will follow Line 2 of Fig. 4, precipitation of both ice and $NaCl{\cdot}2H_2O$ occurs at the −21.1 °C eutectic temperature. Therefore, two frozen samples with different concentrations of NaCl, 1.2 wt. per cent and eutectic (23.16 wt. per cent), were manufactured and their temperatures, thermal conductivities, and calorimetry were measured. The results are compared with the pure water sample introduced in Section 3.1. As mentioned in Section 2, a small sample of the liquid salt-water solution was set aside for the calorimetry measurements.

Fig. 5 shows the thermal conductivity and temperature values measured by thermocouples and thermal conductivity meter for eutectic (23.16 wt. per cent) $NaCl + H_2O$ ice as a function of time. The onset temperature, T_{onset}, corresponds to the start of the peak in the heat flow (mW) measured by the calorimeter, see Fig. 6. This temperature coincides with the start of the crystallization during the freezing process of the solution. The onset temperature, T_{onset}, coincides with the plateau in Fig. 5 between 0 and 20 h where the heat is being released as water ice continuously crystallizes or freezes, which is the result of slowing down the cooling of the water solution. The crystallization would continue to take place until the liquid phase changes completely into solid phase. Furthermore, the temperature at which the first ice starts to melt is referred to as the onset temperature during the melting process. The melting of the ice solution would continue to take place until the solid changes completely into the liquid phase. This corresponds to a long period of constant temperature recorded by the thermocouples due to the endothermic melting in Fig. 5 between 155 and 160 h.

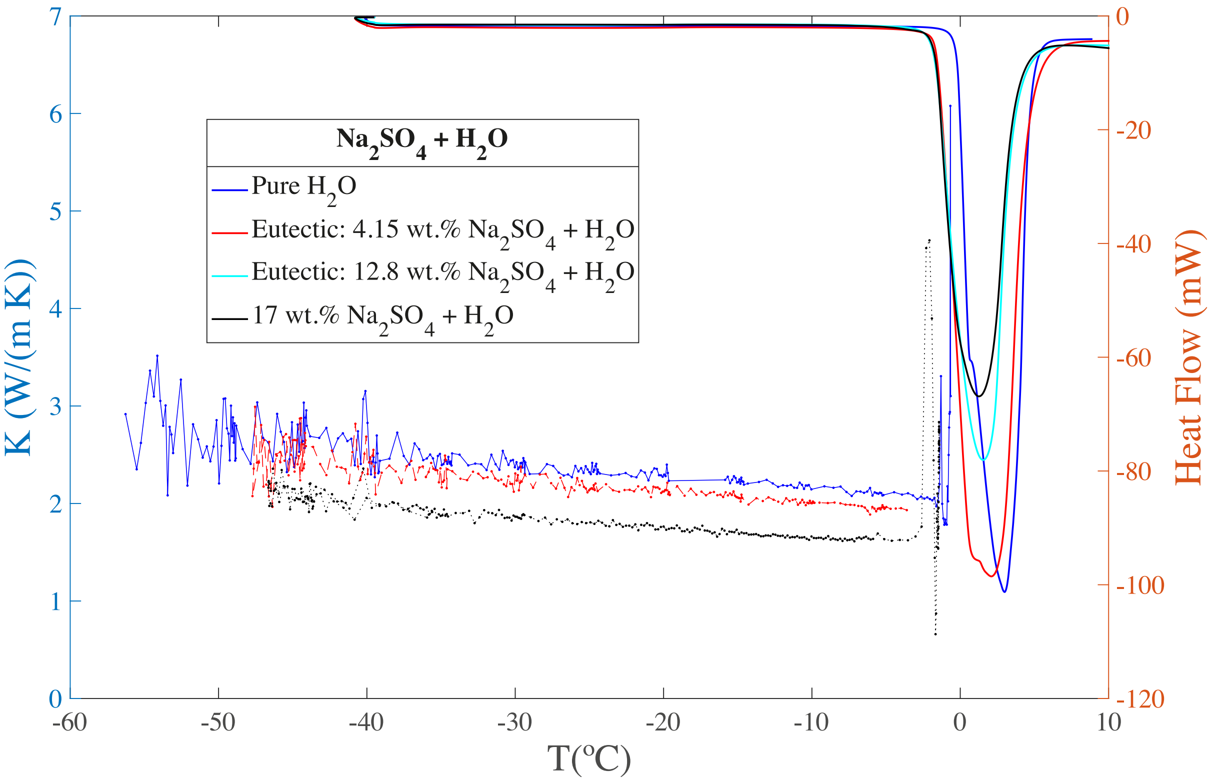

Figure 12. Thermal conductivity (left axis) and calorimetry (right axis) measurements for $Na_2SO_4 + H_2O$ with different Na_2SO_4 concentration. Blue trace is pure H_2O. Red trace is 4.15 wt. per cent $Na_2SO_4 + H_2O$. Black trace is 17 wt. per cent $Na_2SO_4 + H_2O$.

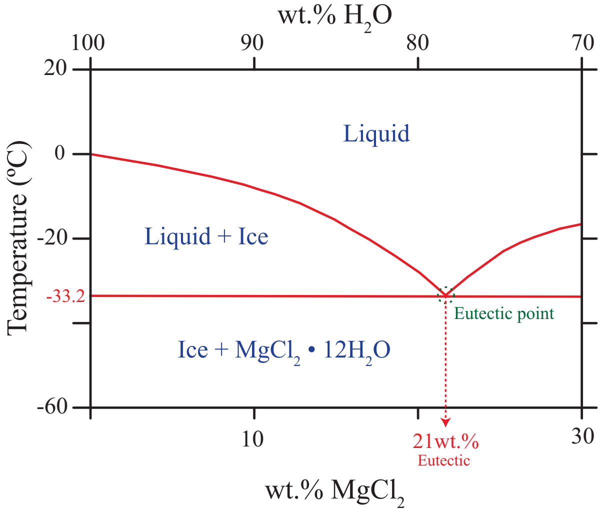

Figure 13. Phase diagram for the $MgCl_2 + H_2O$ solution. Redrawn after Li et al. (2016) and references therein.

From Figs 4 and 6, the following information could be extracted:

(i) Blue line in Fig. 6 (Pure water):

(a) $T_{\rm onset} = -0.21\,^{\circ}C \rightarrow$ 100 per cent water ice (pure H_2O).

(ii) Red line in Fig. 6 (1.2 wt. per cent NaCl $+ H_2O$):

(a) $T_{\rm onset} = -21.8\,^{\circ}C \rightarrow$ 1.2 per cent eutectic mixture hydrohalite (23 wt. per cent $NaCl.H_2O$) + pure water ice (77 wt. per cent water ice H_2O).

(b) $T_{\rm onset} = -2.6\,^{\circ}C \rightarrow$ 98.8 per cent pure water ice.

(iii) Black line in Fig. 6 (23.16 wt. per cent NaCl $+ H_2O$):

(a) $T_{\rm onset} = -23.4\,^{\circ}C \rightarrow$ 100 per cent eutectic mixture hydrohalite (23 wt. per cent $NaCl.H_2O$) + pure water ice (77 wt. per cent water ice H_2O).

It can be noted that around −21 °C there is a peak in the thermal conductivity measurement with NaCl salt concentrations (1.2 wt. per cent and 23 wt. per cent), see Fig. 6. This peak is due to the fact that at this temperature there is a phase change in the NaCl $+ H_2O$ solutions. The heat release in the ice as a consequence of this phase change leads to a false value of the thermal conductivity. This peak is, nevertheless, a sensitive indicator of phase changes in the salt ice. This peak matches the phase diagram of the NaCl $+ H_2O$ system (Fig. 4).

Fig. 6 compares the thermal conductivities and the calorimetry of H_2O and NaCl with different concentrations. It can be appreciated that the thermal conductivity of the eutectic ice mixture 23.16 wt. per cent NaCl $+ H_2O$ (black dots) is slightly different than the thermal conductivity of the other samples, 1.2 wt. per cent NaCl $+ H_2O$ (red dots) and pure water (blue dots), which are very similar to each other. This figure illustrates what has already been pointed out about the calorimetric measurements and the phase diagram of NaCl $+ H_2O$ system: both solutions behave similarly to pure water:

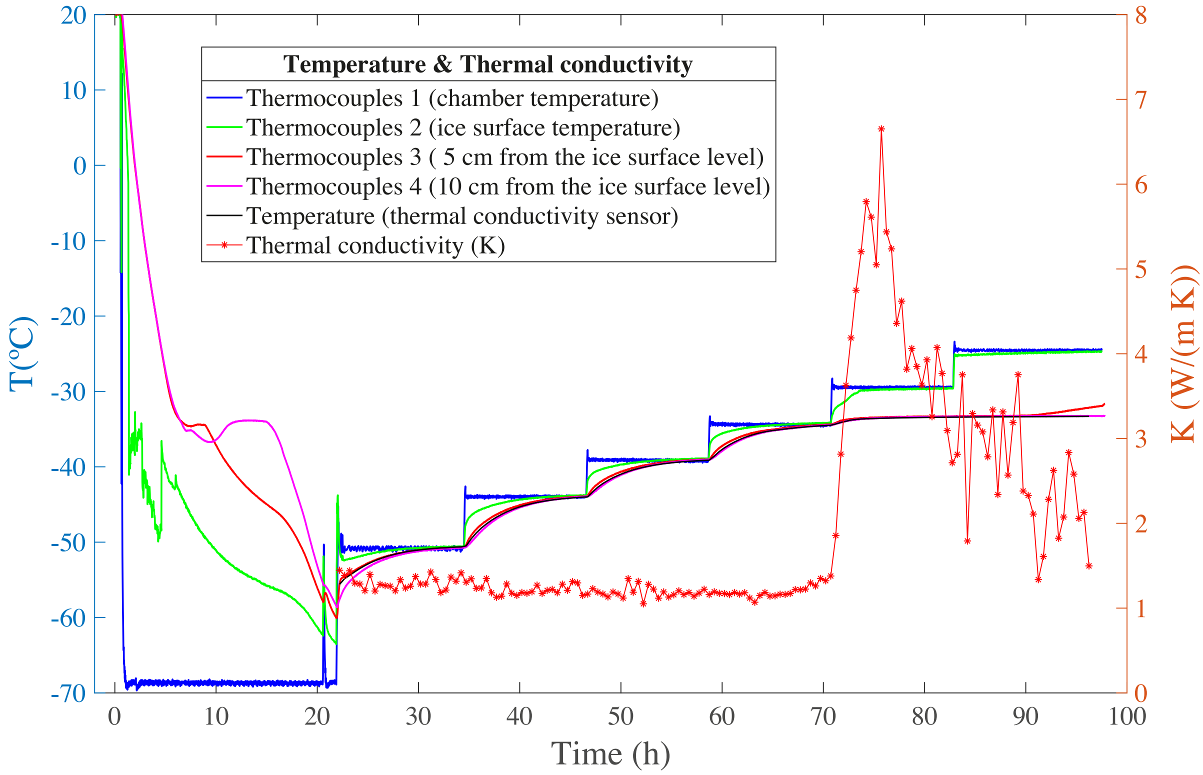

Figure 14. Thermal conductivity (right axis) and temperature (left axis) values measured by thermocouples and thermal conductivity meter for the eutectic (21 wt. per cent) $MgCl_2 + H_2O$ ice as a function of time. To link the temperature values to their corresponding thermal conductivity values, for instance at 100 h, an imaginary vertical line should be projected from the thermal conductivity value to the temperature values on top.

(i) Pure water (H_2O) (blue dots) → 100 per cent water ice + 0 per cent eutectic mixture (23 wt. per cent $NaCl.H_2O$ + 77 wt. per cent H_2O ice).

(ii) 1.2 per cent M NaCl + H_2O (red dots) → 98.8 per cent water ice + 1.2 per cent eutectic mixture (23 wt. per cent $NaCl.H_2O$ + 77 wt. per cent H_2O ice).

3.3 Magnesium sulphate ($MgSO_4$) solution

From the phases diagram in Fig. 7, it could be found that the concentration of the solution will determine which solids precipitate and the temperature at which equilibrium precipitations first occurs. The equilibrium phase diagram of $MgSO_4$, Fig. 7, shows that a dilute solution will precipitate to form ice near 0 °C, while a solution with a eutectic concentration of 17 wt. per cent salt will precipitate both ice and $MgSO_4{\cdot}11H_2O$ at the −3.7 °C eutectic temperature. Therefore, we performed one run using solutions at 17 wt. per cent salt concentration, which is the eutectic composition of the binary system $MgSO_4{\cdot}H_2O$.

Fig. 8 shows the thermal conductivity and the temperature values measured by thermocouples and thermal conductivity meter for $MgSO_4 + H_2O$ ice as a function of time. It can be noted that the steps in this figure are longer that the steps in Fig. 5, taking more time to reach the temperature due to the lower thermal conductivity of this ice mixture. A peak at −3.7 °C in the thermal conductivity measurement (red traces) can be seen. This peak coincides with the phase change from liquid to solid in the $MgSO_4 + H_2O$ ice mixture. The onset temperature obtained from the calorimetry measurement for this sample is $T_{\mathrm{onset}} = -4.48$ °C, see Fig. 9. A comparison of the thermal conductivity and calorimetry results between pure water and the magnesium sulfate sample is shown in Fig. 9. The conductivity values are lower in the mixture with magnesium sulfate than with only pure water.

3.4 Sodium sulphate (Na_2SO_4) solution

Sodium sulphate decahydrate or mirabilite $Na_2SO_4{\cdot}10\,H_2O$ is the stable phase in contact with an equilibrium mixture of Na_2SO_4 and H_2O at room temperature and atmospheric pressure. The eutectic, E_1 in Fig. 10, between mirabilite and ice I_h (hexagonal ice crystal) is at −1.3 °C, 4.15 wt. per cent $Na_2SO_4 + H_2O$. A metastable phase, $Na_2SO_4 \cdot 7\,H_2O$, is known at room temperature and atmospheric pressure. The metastable heptahydrate ice I_h eutectic, E_2 in Fig. 10, is at −3.55 °C, 12.8 wt. per cent Na_2SO_4.

Therefore, a set of three experiments has been performed using E_1 concentration, 4.15 wt. per cent, E_2 concentrations 12.8 wt. per cent and 17 wt. per cent of Na_2SO_4, see Fig. 10. The latter experiment (17 wt. per cent of Na_2SO_4) was performed to check the sensibility of the thermal conductivity measurement during the phase change and the concentration effect on the thermal conductivity.

Fig. 11 shows the thermal conductivity and the temperature values measured by thermocouples and thermal conductivity meter for $Na_2SO_4 + H_2O$ ice as a function of time. The calorimetry measurements in Fig. 12 show that the melting points are quite similar for the three concentrations, 4.15 wt. per cent, 12.8 wt. per cent and 17 wt. per cent, their values fall around −1.5 °C. Therefore, it can be concluded that only stable phase of sodium sulphate decahydrate or mirabilite $Na_2SO_4{\cdot}10\,H_2O$ is formed with 10 water molecules and no evidence of the metastable phase, $Na_2SO_4{\cdot}7\,H_2O$, which would be

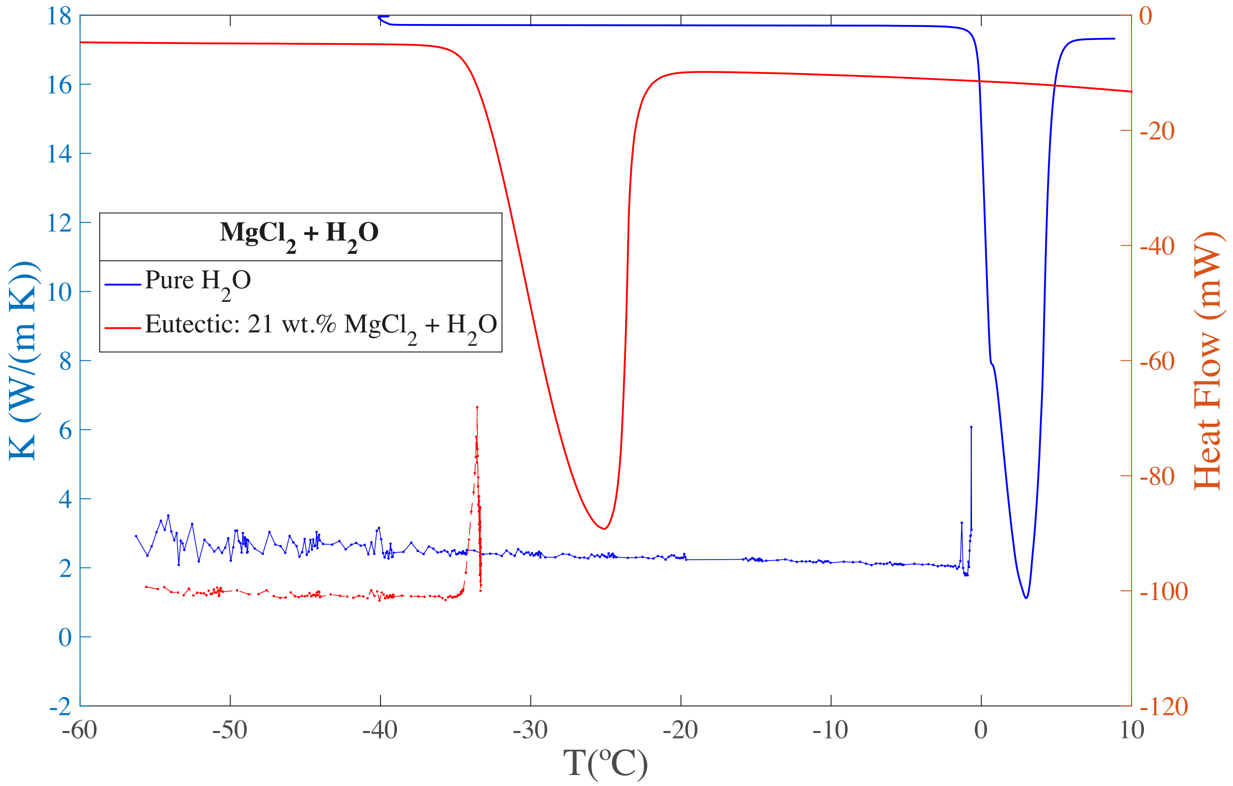

Figure 15. Calorimetry measurements for $MgCl_2 + H_2O$ with the eutectic 21 wt. per cent $MgCl_2$ concentration. Blue trace is pure H_2O. Red trace is eutectic 21 wt. per cent $MgCl_2 + H_2O$.

reflected in a melting point at a lower temperature, around −3.5 °C in the calorimetry measurements, as it can be seen in the phase diagram in Fig. 10. However, in the thermal conductivity measurements, Fig. 12, it could be noted that the peak of the 17 wt. per cent Na_2SO_4 solution is lower than the peak of the 4.15 wt. per cent Na_2SO_4.

(i) $T_{\rm onset1} = -1.37\,^{\circ}$C (4.15 wt. per cent)
(ii) $T_{\rm onset2} = -1.6\,^{\circ}$C (12.8 wt. per cent)
(iii) $T_{\rm onset3} = -1.62\,^{\circ}$C (17 wt. per cent)

3.5 Magnesium chloride ($MgCl_2$) solution

From Fig. 13, the equilibrium phase diagram of $MgCl_2$ shows that a dilute solution will precipitate ice near 0 °C, while a solution with a eutectic concentration of 21 wt. per cent of $MgCl_2$ salt concentration will precipitate both ice and $MgCl_2{\cdot}12H_2O$ at the −33.2 °C eutectic temperature. Therefore, the eutectic stable phase occurs around 21 wt. per cent of $MgCl_2$ salt concentration. Fig. 14 presents the temperature values measured by the thermocouples (left axis) and thermal conductivity (right axis) meter of the eutectic solution as a function of time. This figure shows a peak around −33 °C in the thermal conductivity measurement (red trace with dots). This peak coincides with the phase change from liquid to solid in $MgCl_2 + H_2O$ (Fig. 13).

The $MgCl_2 + H_2O$ system can supercool (Toner, Catling & Light 2014) below its eutectic temperature at −33.2 °C before crystallization occurs. That is, the temperature drops below the freezing point for some time, as shown by the little dip in the cooling curve, magenta trace, of Fig. 14 between 7 and 12 h, below −33.2 °C. This region corresponds to an unstable form of the magnesium chloride ($MgCl_2$) solution, it does not crystallize well, it solidifies in a disorganized way, and it does so at temperatures well below freezing. If the magnesium chloride ($MgCl_2$) solution is allowed to stand, if cooling is continued, or if a small crystal of the solid phase is added (a seed crystal), the supercooled liquid solution will convert to a solid, sometimes quite suddenly. As the solution freezes, the temperature increases slightly due to the heat evolved during the freezing process and then holds constant at the melting point as the rest of the solution freezes. Therefore, it needs to be supercooled to crystallize well. The calorimeter used for the previous experiments can only cool down to −40 °C, which explains why in our previous attempts (not shown in this paper) only water ice crystallized. Hence, a longer cycle and heating ramp at 0.5 K/min was selected, instead of 1 K/min as in the previous experiments. It appears that melting at −33 °C is finally observed, and water ice at 0 °C is also evident. The eutectic at −33 °C is not very well defined, this may be due to the fact that the salt solution did not crystallize well and partially remained as an amorphous phase, or because the reaction is highly exothermic and therefore gives off a lot of heat. As previously mentioned, the thermal transitions were analysed by DSC on a Mettler Toledo DSC 822e calorimeter (Schwerzenbach) equipped with a liquid nitrogen accessory, see Fig. 15. In this case, the sample was cooled from 25 °C to −90 °C at a rate of 10 °C/min, maintained for 7 min at this temperature and reheated from −90 °C to 25 °C at a rate of 10 °C/min. The calorimetry measurements for the eutectic 21 wt. per cent $MgCl_2 + H_2O$ (red trace) and pure water (blue trace) are shown in Fig. 15.

4 DISCUSSION

Fig. 16 shows a summary of the thermal conductivity (bottom panel) and calorimetry (top panel) measurements for H2O (blue trace),

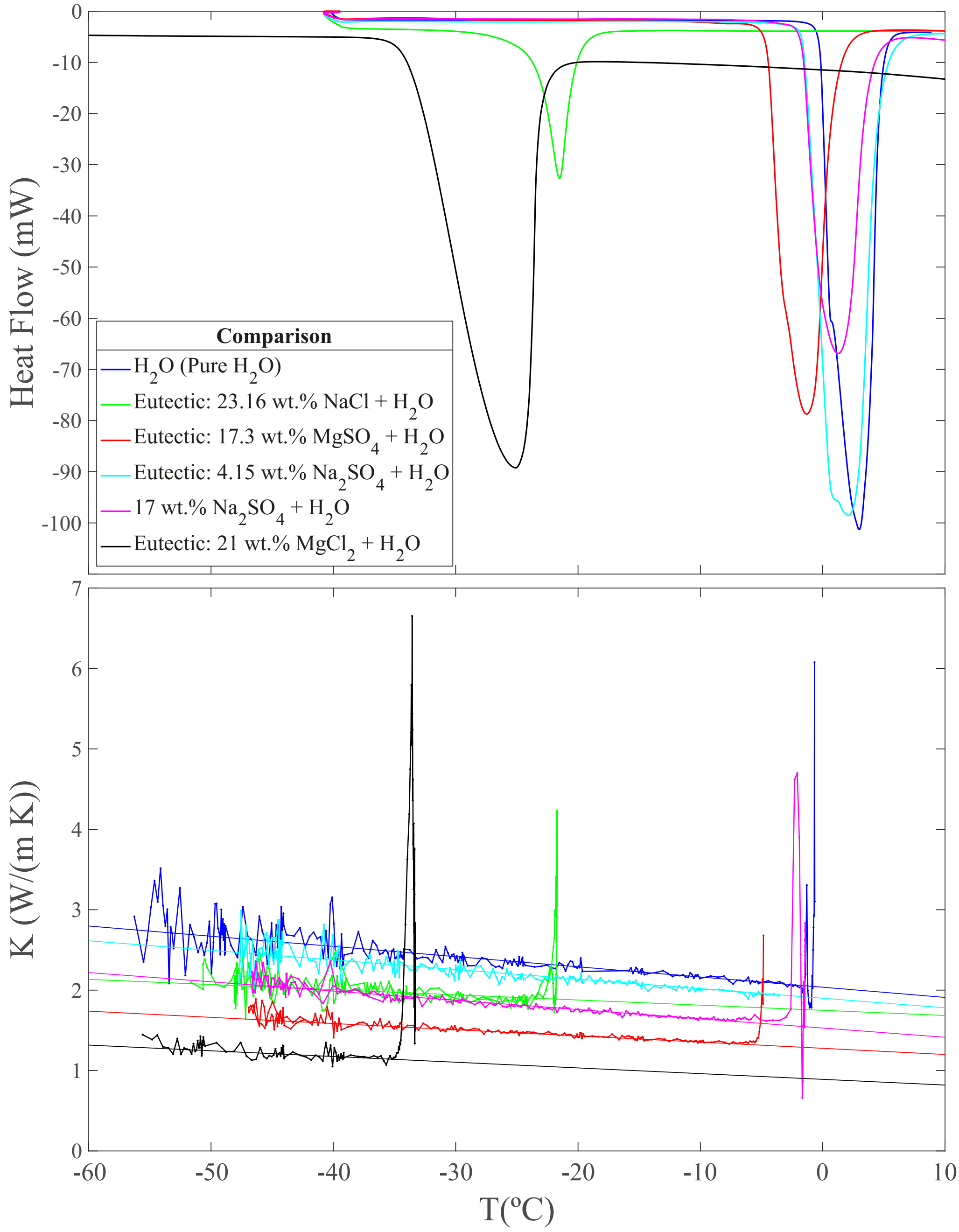

Figure 16. Thermal conductivity and calorimetry measurements for H_2O (blue trace), eutectic 23.16 wt. per cent NaCl + H_2O (green trace), eutectic 17.3 wt. per cent $MgSO_4$ + H_2O (red trace), eutectic 4.15 wt. per cent Na_2SO_4 + H_2O (cyan trace), 17 wt. per cent Na_2SO_4 + H_2O (magenta trace), and eutectic 21 wt. per cent $MgCl_2$ + H_2O (black trace). Fit type: linear: a∗T + b.

eutectic 23.16 wt. per cent NaCl + H_2O (green trace), eutectic 17.3 wt. per cent $MgSO_4$ + H_2O (red trace), eutectic 4.15wt. per cent Na_2SO_4 + H_2O (cyan trace), 17 wt. per cent Na_2SO_4 + H_2O (magenta trace), and eutectic 21 wt. per cent $MgCl_2$ + H_2O (black trace).

A conclusion of this work is that the sensitivity of our conductivity measurements served to identify phase changes, as a sudden rise of the conductivity forming a sharp peak that reaches values above the range of the thermal conductivity sensor, 4 W/(m·K). The peak value is not the real value of the conductivity, but it serves to spot phase changes. These peaks are caused by a change in the temperature during the phase change that the sensor interprets as a large variation of the thermal conductivity. In addition, for solutions at the phase change temperature, convection induces temperature variations and the thermal conductivity measurements may have large uncertainties. Sometimes this method was more sensitive than the calorimeter itself to identify phase changes. As an example, we refer to Fig. 6 where a peak in the thermal conductivity is measured, even with 0.6 wt. per cent concentration of NaCl, a very low value, while the calorimeter did not detect a phase change.

Fig. 16 illustrates that the thermal conductivity of the macroscopic ice samples grown for this study are different from each other.

Table 2. Summary of the literature (phase diagrams) and experimental (thermal conductivity sensor and calorimetry experiments) phase change freezing temperatures and linear fitting values for the different salt systems reported in this paper.

Salt system	$T_{freezing}$ Phase change (°C)			Linear Fit	
	Phase Diagram	Thermal conductivity sensor experiment	Calorimetry experiment (T_{onset})	a∗T + b	
Pure Water	0	−0.669	−0.211	−0.01268 R = 0.98	5.5
NaCl (21 wt. per cent)	−21.1	−21.7	−23.41	−0.00641 R = 0.98	3.5
$MgSO_4$ (17.3 wt. per cent)	−3.7	−4.84	−4.48	−0.0077 R = 0.99	3.38
Na_2SO_4 (4.15 wt. per cent)	−1.3		−1.374	−0.0119 R = 0.99	5.15
Na_2SO_4 (17 wt. per cent)	−3.5	−2.08	−1.629	−0.0115 0.99	4.67
$MgCl_2$ (21 wt. per cent)	−33.2	−33.66	-33.42	−0.0071 R = 0.96	2.83

However, all thermal conductivities share similarities, such as the slope values of the thermal conductivity (Fig. 16 and Table 2) as a function of the temperature which varies from 1 to 3 W/(m·K). In all cases, we can see a similar linear trend of thermal conductivity as a function of the temperature. A very interesting fact is that the salts lower the thermal conductivity, which means that the thermal gradients will be weaker if there are salts and that the heat is lost more slowly. It can also be seen that certain solutions are more similar to each other, such as pure water and 4.15 wt. per cent sodium sulphate (4.15 wt. per cent $Na_2SO_4 + H_2O$) with $a_{H_2O} = -0.01268$ and $a_{Na_2SO_4} = -0.0119$, or 23.16 wt. per cent Na-chloride (23.16 wt. per cent NaCl) and 17.3 wt. per cent sodium sulphate (17.3 wt. per cent $Na_2SO_4 + H_2O$) with slightly different slope values of −0.00641 and −0.0077, respectively. In the temperature range studied, −55 to 0 °C, the range of the thermal conductivity goes from 1 W/(m·K) for the eutectic 21 wt. per cent magnesium chloride (21 wt. per cent $MgCl_2 + H_2O$) at around −33 °C to 3 W/(m·K) for the pure water (H_2O) at around −55 °C. Therefore, the highest values of thermal conductivity correspond to pure water (H_2O) (blue trace in Fig. 16) and the lowest values to the 21 wt. per cent magnesium chloride (21 wt. per cent $MgCl_2 + H_2O$), the black trace in Fig. 16.

The results for the various phases, states, and the temperature range studied are in most cases described well by the linear equation used in this paper: $k = a \cdot T + b$. In the literature, numerous fitting adjustments for the experimental thermal conductivity data have been found, such as the one used by Andersson & Inaba (2005), $k = a/T + b + c \cdot T$, Slack (1980), $k = a/T$, or linear fitting (Bonales et al. 2017, and references therein). However, in all these cited cases, the thermal conductivity data are for pure H_2O ice (Andersson 2018; Wolfenbarger et al. 2021).

Our data are in agreement with slurry ice (Melinder 2003) where the higher conductivity of ice compared to the liquid phase enhances the thermal conductivity of the system. Indeed, this author reports the thermal conductivity of ice slurries is clearly higher than that of single-phase aqueous solutions.

5 ASTROPHYSICAL IMPLICATIONS AND CONCLUSIONS

In this paper, we provide measurements of temperature, calorimetry, and thermal conductivity in ice analogues containing salts with different concentrations as input for the thermodynamical models of Jovian icy moons that will be developed to interpret the volume of data from these missions. These measurements of thermal conductivity and calorimetry for relevant salt solutions are expected to be useful to better constrain the chemical composition, physical state, and temperature of the upper layers of Ganymede, Europa, and Callisto. Indeed, there is a significant lack of literature regarding the thermal properties of frozen salt solutions.

The surfaces of these icy moons are exposed to cometary and meteoritic impacts. In particular, embedded micro-meteoroids may be relatively abundant in the icy crust and contribute to the thermal conductivity of the moon surfaces. However, the thermal conductivity values of meteorites cover a wide range, from 0.5 W/(m·K) in carbonaceous chondrites to more than 10 W/(m·K) in iron meteorites, and these values can strongly depend on temperature (Opeil, Consolmagno & Britt 2010).

The MAJIS (Moons and Jupiter Imaging Spectrometer) instrument onboard JUICE will perform visible-IR spectroscopy in the 0.4–5.7 μm range, with spectral resolution of 3–7 nm to characterize the composition and physical properties of these satellite's surfaces. The spatial resolution will be up to 25 m on Ganymede and about 100 km on Jupiter. The spectral resolution of MAJIS will be about 4 times better than the Galileo/Near-Infrared Mapping Spectrometer in the near-infrared range (better than 7 nm/band between 2.25 and 5.54 μm), providing a data quality closer to lab spectra of several non-ice materials measured at temperatures representative of the icy Galilean satellites (Piccioni et al. 2019). The ices, salts, minerals, and organic materials will be observed in this spectral range. This mapping of the surface composition will serve to better understand the geological history of these moons. MAJIS has the capability to analyse the composition of non-water ice components and determine the state and crystallinity of water ice; for more information, see JUICE Red Book available online at https://sci.esa.int.

Mapping of the moon temperatures will be provided by the Sub-millimeter Wave Instrument, along with the measurement of thermophysical and electrical properties of their surface/subsurface. The RIME (Radar for Icy Moons Exploration) instrument employs radar sounding to study subsurface structures of icy shells with 50–140 m resolution. GIS (Geographic Information System) system will combine spatially referenced information such as imaging, composition, sub-surface, topography, thermal and geophysical data to get a full picture of each moon. Using our data set, which could be extended to lower temperatures in the near future with the design of a new thermal conductivity meter, the heat transfer and temperature in stratified moon (sub)surfaces can be simulated provided that the thickness, composition, and structure of the different salt ice layers are characterized during the JUICE mission.

ACKNOWLEDGEMENTS

This project received financial support of The European Space Agency (ESA) contracts No.: RFP/3-15589/18/ES/CM and 4000126441/19/ES/CM: 'Measurements of thermal and dielectric properties of ices in support to future radar measurements of Jovian Icy moons', The Unidad de Excelencia 'María de Maeztu' MDM-2017-0737– Centro de Astrobiología (INTA-CSIC), The Spanish Ministry of Science, Innovation and Universities AYA2017-85322-R and PID2020-118974GB-C21 (AEI/FEDER, UE), Retos Investigación BIA2016-77992-R (AEI/FEDER, UE), and 'Explora Ciencia y Explora Tecnología' [AYA2017-91062-EXP]. We are grateful to Anezina Solomonidou for assistance in the project proposal. The view expressed in this article can in no way be taken to reflect the official opinion of the European Space Agency. We thank the reviewer of this article for his constructive comments.

DATA AVAILABILITY

The data underlying this article cannot be shared publicly.

REFERENCES

Anderson J., Jacobson R., McElrath T., Moore W., Schubert G., Thomas P., 2001, Icarus, 153, 157
Andersson O., 2018, J. Chem. Phys., 149, 124506
Andersson O., Inaba A., 2005, J. Chem. Phys., 7, 1441
Bonales L. J., Rodriguez A. C., Sanz P. D., 2017, Int. J. Food Prop., 20, 610
Brand H. E. A., Fortes A. D., Wood I. G., Knight K. S., Vocadlo L., 2009, Phys. Chem. Miner., 36, 29
Cameron M. E., Smith-Konter B. R., Burkhard L., Collins G. C., Seifert F., Pappalardo R. T., 2018, Icarus, 315, 92
Carey E. M., Vu T., Choukroun M., Zhong F., Cohen B., Barmatz M., Zimmerman W., Cwik T., 2018, in 49th Lunar and Planetary Science Conference, Lunar and Planetary Science Conference. The Woodlands, Texas LPI, p. 2871
Carlson R. W. et al., 1996, Science, 274, 385
Carlson R. W. et al., 1999a, Science, 283, 2062
Carlson R. W., Johnson R. E., Anderson M. S., 1999b, Science, 286, 97
Chou I.-M., Seal R. R., Wang A., 2013, J. Asian Earth Sci., 62, 734
Clark R., 1980, Icarus, 44, 388
Collins G. C., Head J. W., Pappalardo R. T., 1998, Icarus, 135, 345
Dalton J., Prieto-Ballesteros O., Kargel J., Jamieson C., Jolivet J., Quinn R., 2005, Icarus, 177, 472
Dalton J., Cassidy T., Paranicas C., Shirley J., Prockter L., Kamp L., 2013, Planet. Space Sci., 77, 45
Fink U., Dekkers N., Larson H., 1973, ApJ, 179, L155
Golombek M. P., Allison M. L., 1981, Geophys. Res. Lett., 8, 1139
Grasset O. et al., 2013, Planet. Space Sci., 78, 1
Greeley R., Klemaszewski J. E., Wagner R., Galileo Imaging Team, 2000, Planet. Space Sci., 48, 829
Hansen G. B., McCord T. 2008, Geophys. Res. Lett., 35, L01202
Heggy E., Scabbia G., Bruzzone L., Pappalardo R. T., 2017, Icarus, 285, 237
Hendrix A. R., Barth C. A., Hord C. W., 1999, J. Geophys. Res.: Planets, 104, 14169
Kargel J. S., 1991, Icarus, 94, 368
Kargel J. et al., 2000, Icarus, 148, 226
Kivelson M., Khurana K., Volwerk M., 2002, Icarus, 157, 507
Klinger J., 1980, Science, 209, 271
Kuskov O., Kronrod V., 2005, Icarus, 177, 550
Li D., Zeng D., Yin X., Han H., Guo L., Yao Y., 2016, Calphad, 53, 78
Lin W., Dalmazzone D., Fürst W., Delahaye A., Fournaison L., Clain P., 2013, J. Chem. Thermodyn., 61, 132
McCord T. et al., 1997, Science, 278, 271
McCord T. et al., 1998a, J. Geophys. Res. E: Planets, 103, 8603
McCord T. B. et al., 1998b, Science, 280, 1242
McCord T., Hansen G., Hibbitts C., 2001, Science, 292, 1523
Marion G., Kargel J., Catling D., Jakubowski S., 2005, Geochim. Cosmochim. Acta, 69, 259
Melinder A., 2003, 21st International Congress of Refrigeration. IIR/IIF Washington
Noll K. S., Johnson R. E., Lane A. L., Domingue D. L., Weaver H. A., 1996, Science, 273, 341
Opeil C., Consolmagno G., Britt D., 2010, Icarus, 208, 449
Orlando T. M., McCord T. B., Grieves G. A., 2005, Icarus, 177, 528
Pappalardo R. T. et al., 1998, Icarus, 135, 276
Parmentier E. M., Squyres S. W., Head J. W., Allison M. L., 1982, Nature, 295, 290
Patterson G. W., Collins G. C., Head J. W., Pappalardo R. T., Prockter L. M., Lucchitta B. K., Kay J. P., 2010, Icarus, 207, 845
Pettinelli E., Cosciotti B., Di Paolo F., Lauro S., Mattei E., Orosei R., Vannaroni G., 2015, Rev. Geophys., 53, 593
Piccioni G. et al., 2019, in 2019 IEEE 5th International Workshop on Metrology for AeroSpace (MetroAeroSpace). Scientific goals and technical challenges of the MAJIS imaging spectrometer for the JUICE mission, IEEE, Turin, Italy, p. 318
Prieto-Ballesteros O., Kargel J. S., Fernández-Sampedro M., Selsis F., Martínez E. S., Hogenboom D. L., 2005, Icarus, 177, 491
Prockter L., Pappalardo R., Head III J., 2000, J. Geophys. Res. E: Planets, 105, 9483
Roth L., Saur J., Retherford K. D., Strobel D. F., Feldman P. D., McGrath M. A., Nimmo F., 2014, Science, 343, 171
Schenk P. M., 1993, J. Geophys. Res.: Planets, 98, 7475
Schenk P. M., 1995, J. Geophys. Res.: Planets, 100, 19023
Schenk P., 2002, Nature, 417, 419
Showman A. P., Malhotra R., 1999, Science, 296, 77
Showman A. P., Mosqueira I., Head J. W., 2004, Icarus, 172, 625
Slack G. A., 1980, Phys. Rev. B, 22, 3065
Sohl F., Choukroun M., Kargel J., Kimura J., Pappalardo R., Vance S., Zolotov M., 2010, Space Sci. Rev., 153, 485
Sparks W. B., Hand K. P., McGrath M. A., Bergeron E., Cracraft M., Deustua S. E., 2016, ApJ, 829, 121
Toner J., Catling D., Light B., 2014, Icarus, 233, 36
Wolfenbarger N. S., Carnahan E., Jordan J. S., Hesse M. A., 2021, Data Brief, 36, 107079
Zimmer C., Khurana K. K., Kivelson M. G., 2000, Icarus, 147, 329

This paper has been typeset from a TEX/LATEX file prepared by the author.